Supplementary material for "Coarsening of fluvial sediments after the Gorkha Earthquake 2015, Nepal"

David Puhl[1,2], Jens M. Turowski[2], Christoff Andermann[3,2], Michael Dietze[4,2], Kristen L. Cook[5], Gen K. Li[6], Basanta R. Adhikari[7]

[1]Department of Geography, University of British Columbia,Vancouver, BC, Canada
[2]Section 4.6 Geomorphology, German Research Centre for Geosciences GFZ, Helmholtzzentrum Potsdam, Telegrafenberg, 14473 Potsdam, Germany
[3]Univ Rennes, CNRS, Géosciences Rennes, UMR 6118, 35000 Rennes, France
[4]Department of Geography, RWTH Aachen University, Wüllnerstraße 5b, D-52062 Aachen, Germany
[5]ISTerre, Université Grenoble Alpes, IRD, Grenoble, France
[6]Department of Earth Science, University of California, Santa Barbara, CA 93106, USA
[7]Department of Civil Engineering, Pulchowk Campus, Institute of Engineering, Tribhuvan University, Nepal

1. Sampling location

The location of all grain size sample locations from debris flow, fluvial, and landslide deposits are shown in the map below. Please refer to figure 1 in the main text for location reference and the methods section outlining sampling procedure. All samples were taken in the Bhotekoshi catchment. Sample locations were selected partly based on accessibility, with steep terrain restricting sampling primarily to landslides near the valley floor.

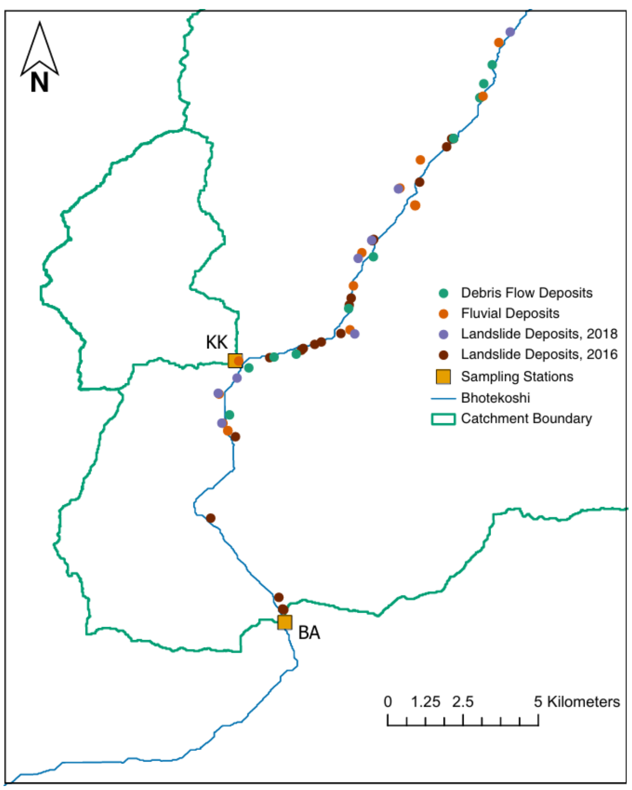

Figure S1: Sampling locations of sediment sources in the Bhotekoshi catchment. KK stands for Kahule Khola and BA for Bhotekoshi. Please refer to Fig. 1 in the main text for location reference.

2. Landslide connectivity

To analyze the impact of landslide density and distribution within our nested catchment approach we performed a simple connectivity analysis. All calculations were performed in QGIS. For stations Kahule Khola, Bhotekoshi, and Sunkoshi we calculated the distance of each landslide to the nearest channel following the flow direction. Additionally, within each catchment we calculated the distance of each landslide to the respective sampling station following the flow direction to the nearest channel as calculated in the first step and along the channel network to the sampling station. We did forego these calculations for the Saptakoshi catchment due to a low landslide density in comparison to the other study catchments (see Table 1 in the main text) and long computational times.

Median distance of landslides to channels in the Kahule Khola are 722 m, while 25 % are 270 m or less away from the nearest channel (Fig. S3 A). Generally, distances from landslides to channels look comparable across all stations, whereas median distance of landslides to channels seems greater for Bhotekoshi and Sunkoshi compared to Kahule Khola exhibiting a 29% and 23% increase, respectively (Fig. S3).

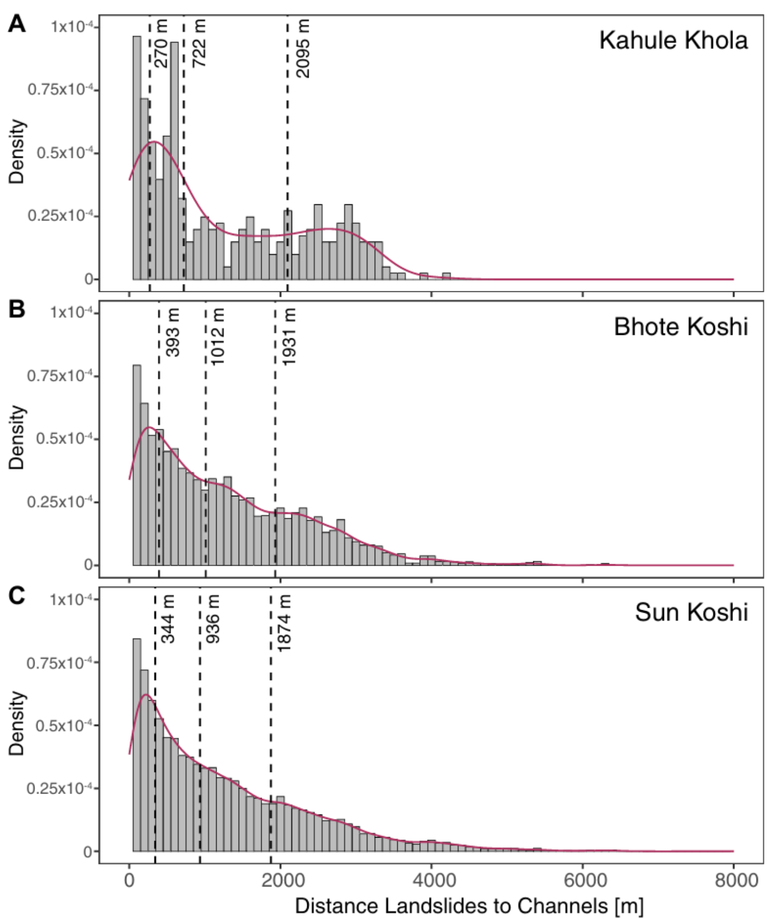

Figure S2: Distance of landslides to nearest channel along the flow direction. A to C show distributions binned by 100 m for each catchment. Dashed lines indicated 25th, 50th, and 75th percentile.

In contrast, distributions of distances between landslides and respective sampling stations differ greatly among the three catchments. Median distance varies from 4.7 km at the Kahule Khola station, to 16.9 km at the Bhotekoshi catchment, to 101 km at the Sunkoshi station (Fig. S4).

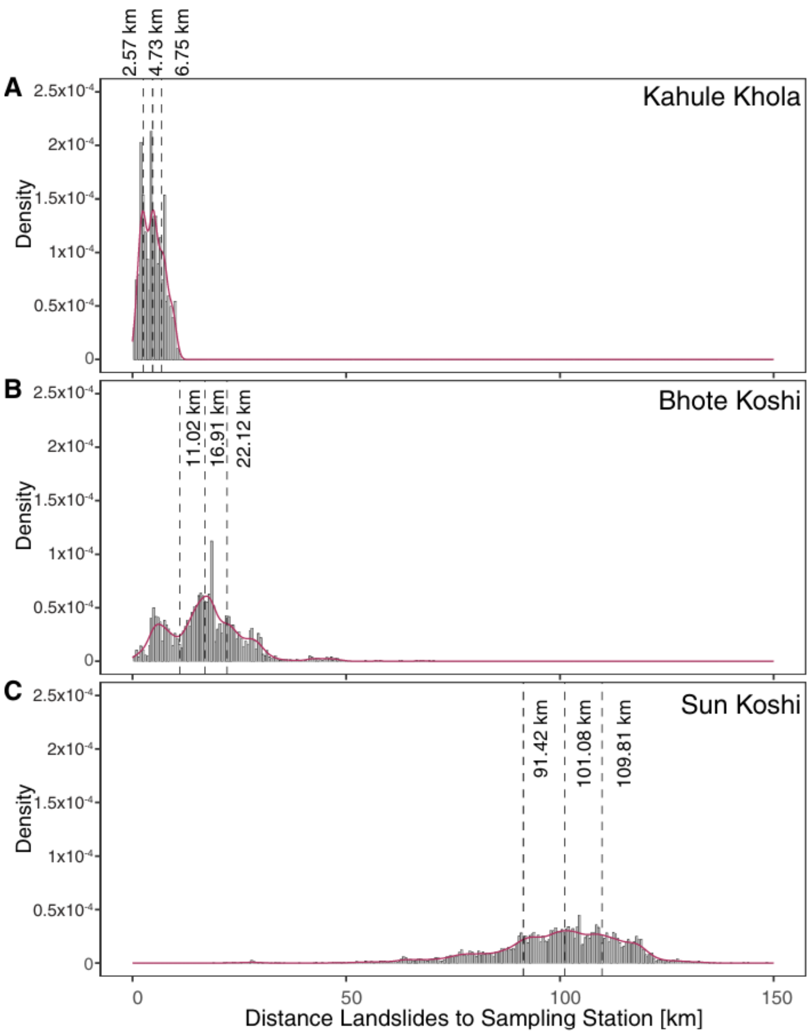

Figure S3: Distance of landslides to hydrometric sampling station. A to C shows binned distribution by 500 m for each station. Dashed lines indicate 25th, 50th, and 75th percentile.

2. Lithology of landslide deposits

Table S1 presents underlying bedrock of all co-seismic landslides during the Gorkha Earthquake. Bedrock information has been derived from a simplified geological map of Nepal published by the British Geological Survey (2022).

Table S1: Underlying geology of landslides

	Granite and Gneiss	Dolomite	Schist	Phyllite	Shale	Quartzite
Kahule Khola	41%	52%	7%	-	-	-
Bhotekoshi	58%	24%	-	9%	2%	6%
Sunkoshi	76%	9%	6 %	4%	1%	4%
Saptakoshi	76%	9%	6%	4%	1%	4%

All landslide samples from 2018 (Fig. S1) and 2015 (Fig. S2) as well as debris flow deposits have been plotted as distribution curves color coded for distinct lithologies.

Gran size distributions vary across all landslide samples in 2015 from a D_{50} of 26 to 123 µm, whereas samples of the same lithology also show variations. Samples underlying granite and gneiss range in D_{50} from 43 to 130 µm, dolomite samples range 27 to 81 µm, and phyllite samples range from 26 to 113 µm (Fig. S2). We ran a Pearson Chi squared which yielded a p value of >0.05, hence no statistical significance between lithologies could be observed. However, to account for the multivariate nature of this data set we additionally performed a PERMANOVA test (Anderson, 2017). This test revealed that lithological category explained 13.9% of the variation in grain-size distributions, but this effect was not statistically significant (Bray–Curtis dissimilarity, $p = 0.513$). Group dispersions were homogeneous (permutational test of multivariate dispersion, $p = 0.272$).

Similarly, landslide deposits sampled in 2018 are underlying granite, dolomite, phyllite, and quartzite. Size distributions range from a D_{50} of 55 to 278 µm. Samples underlying granite range in D_{50} from 91 to 278 µm and dolomite samples range from 56 to 106 µm (Fig. S3). Singles samples of phyllite and quartzite show D_{50}s of 104 µm and 55 µm. For these grain size distributions, a Pearson's Chi-squared test indicated no statistical significance ($p > 0.05$) between lithologies. While based on the PERMANOVA test, lithology explained 48 % of the variation in grain size distributions, but not statistically significant (Bray–Curtis dissimilarity, $p = 0.318$). Tests for homogeneity of multivariate dispersion were also non-significant, although dispersion differed marginally among groups ($p = 0.078$), suggesting some variation in within-group heterogeneity.

Debris flow deposits range in size from D50 84 to 1201 µm, underlying granite and gneiss, dolomite, and quartzite. Samples sourced from granite range in D50 from 160 to 393 µm, while dolomite samples range in D50 from 85 to 128 µm. A single sample of debris flow deposits underlying quartzite shows a D50 of 84 µm. A Person's Chi-squared test suggested no significance of grain size distributions between lithologies ($p > 0.05$) While a PERMANOVA test suggested that lithology explained 54.6 % of variance is explained by lithology as is statistically significant (Bray–Curtis dissimilarity, $p = 0.011$). Tests for homogeneity of multivariate dispersion were non-significant (permutational test of dispersion, $p = 0.330$), indicating that the observed differences reflect shifts in grain-size distributions among lithological categories rather than differences in within-group variability.

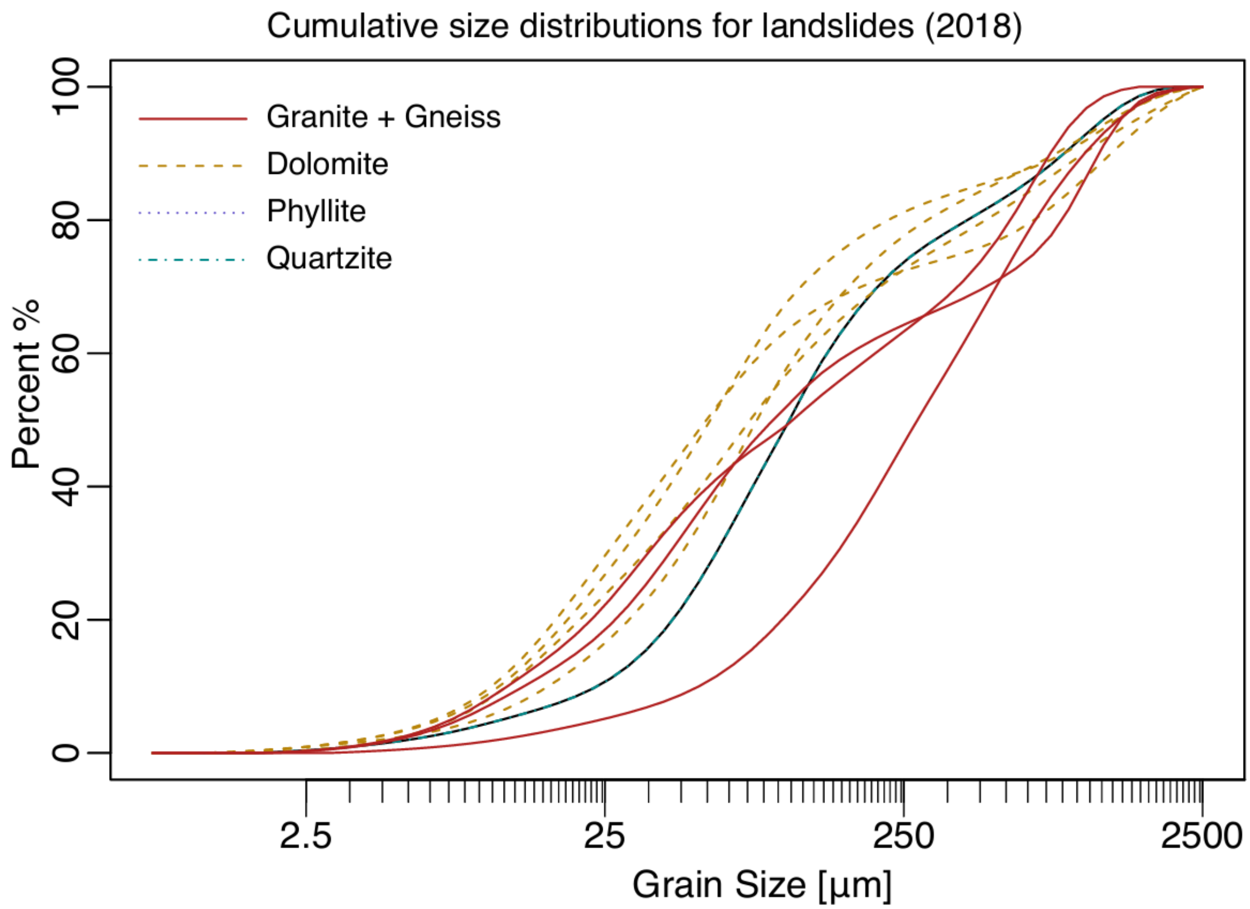

Figure S4: Cumulative size distributions for different landslide deposits sampled in 2018 based on underlying bedrock.

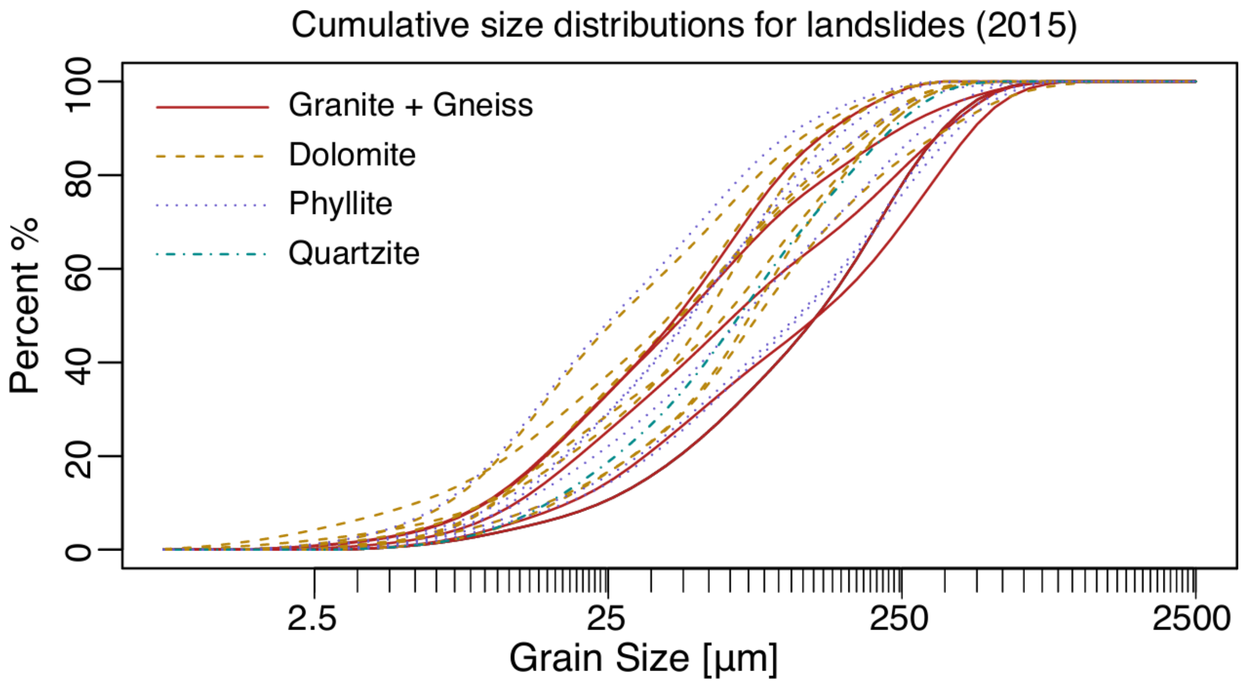

Figure S5: Cumulative size distributions for different landslide deposits sampled in 2015 based on underlying bedrock.

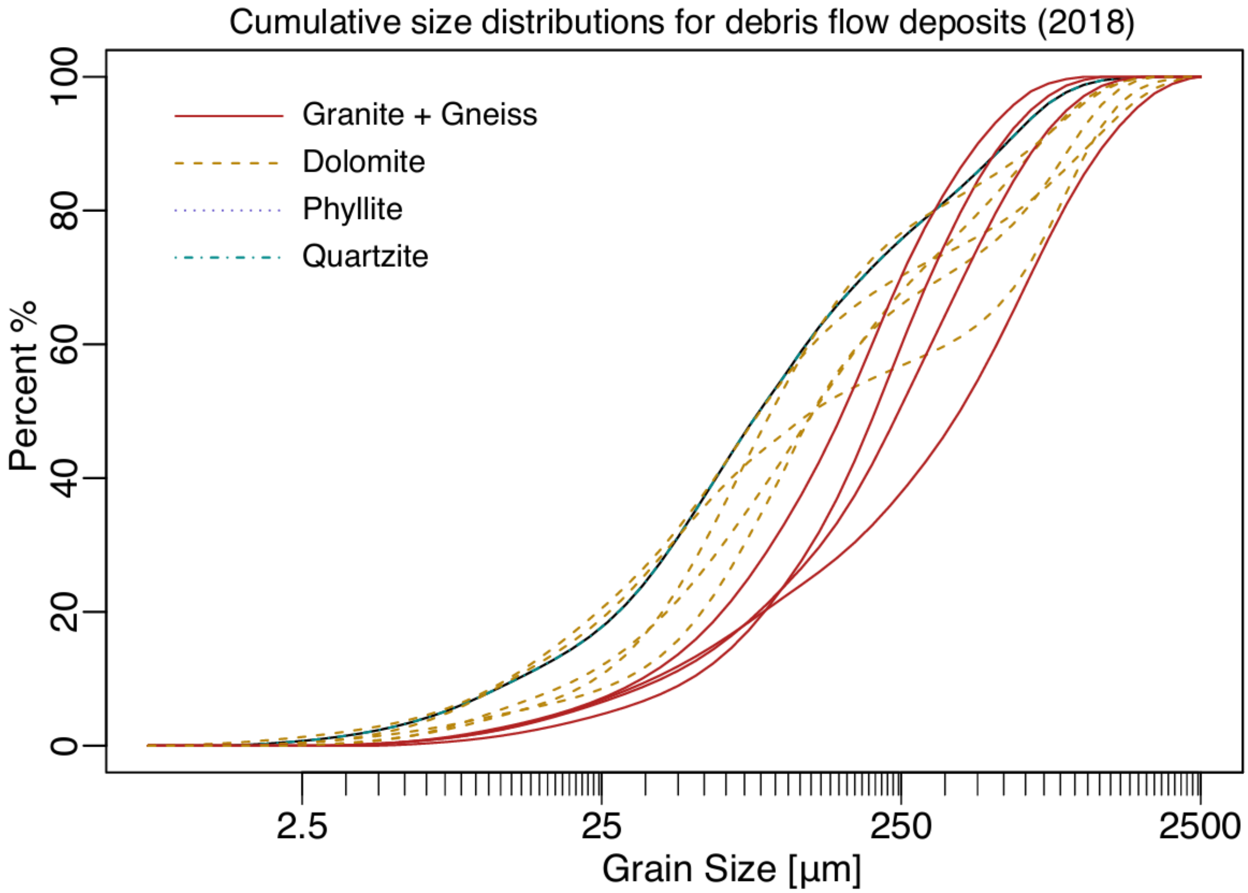

Figure S6: Cumulative size distributions for different debris flow deposit samples based on underlying bedrock.

2. Sediment rating curves

Relationships between discharge and sediment concentration have been developed for Sunkoshi and Saptakoshi stations, where discharge data was available. Relations are shown for individual years (Figs. S4 and S6) and for the entire sampling period (S5 and S7).

Sunkoshi power law relations show minimal variations in scaling exponent from 2015 to 2017, however in 2018 exponent decreases indicating a weakening of sediment load with increase discharge (Fig. S4). The post-earthquake year exhibits generally higher concentrations at similar discharges compared to the following years. Concentrations during monsoons from 2016 to 2018 are present on the rising and falling limb, whereas concentrations in 2015 show high concentration (Fig. S4). Generally, the monsoon in 2015 had higher concentrations at the same discharges than during monsoons in the years 2016, 2017, and 2018 (Fig. S5).

Differences in absolute concentrations to discharges are less pronounced at Saptakoshi comparing the post-earthquake year 2015 to following years (Fig. S6). Moreover, there is generally a weaker scaling with increasing discharge to sediment concentration as observed at Sunkoshi. Scaling exponents do slightly increase from 2015 to 2017 (Fig. S6). Sediment concentration exhibits high variability to similar discharge values across the observation period, however still during the post-earthquake monsoon 2015 concentrations tend to be higher than in the following monsoons 2016 and 2017 (Fig. S7).

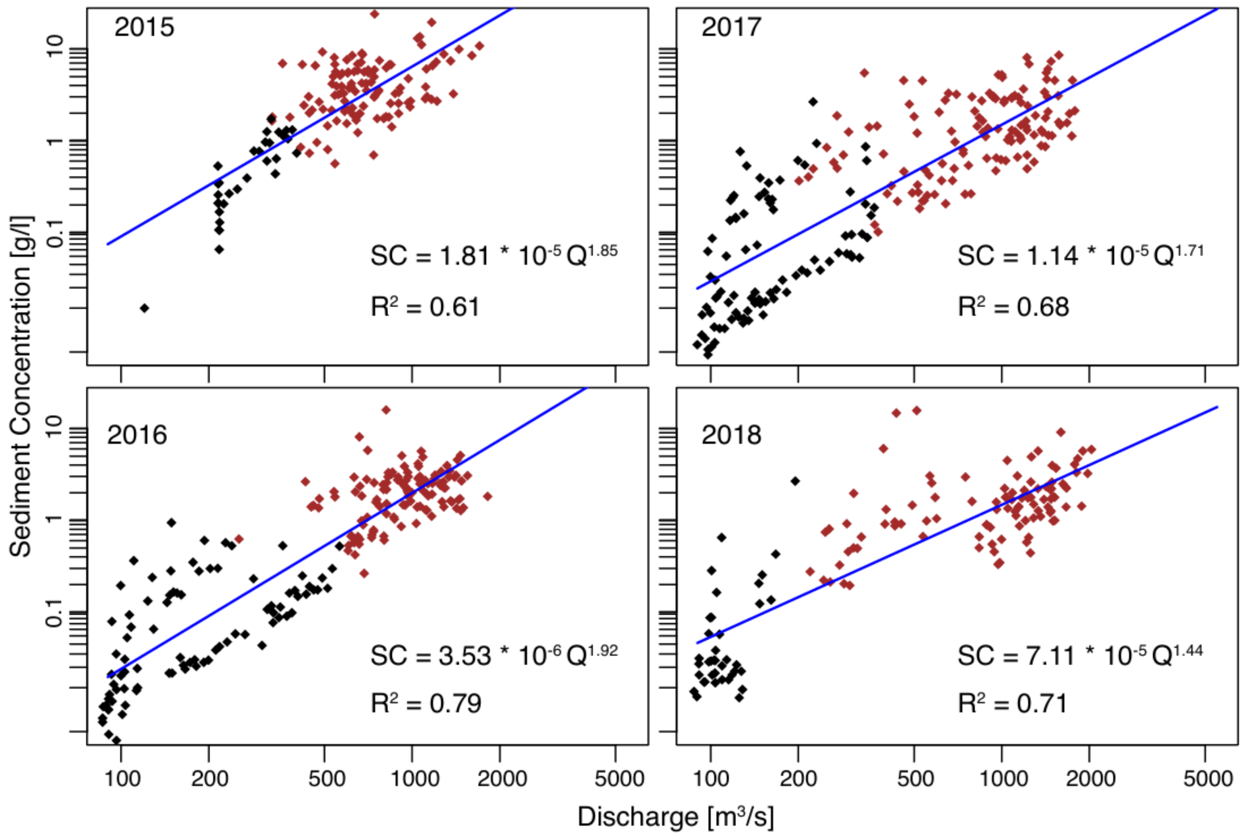

Figure S7: Relationship between sediment concentration and discharge for Sunkoshi sampling station. Red dots indicate samples taken during the monsoon period.

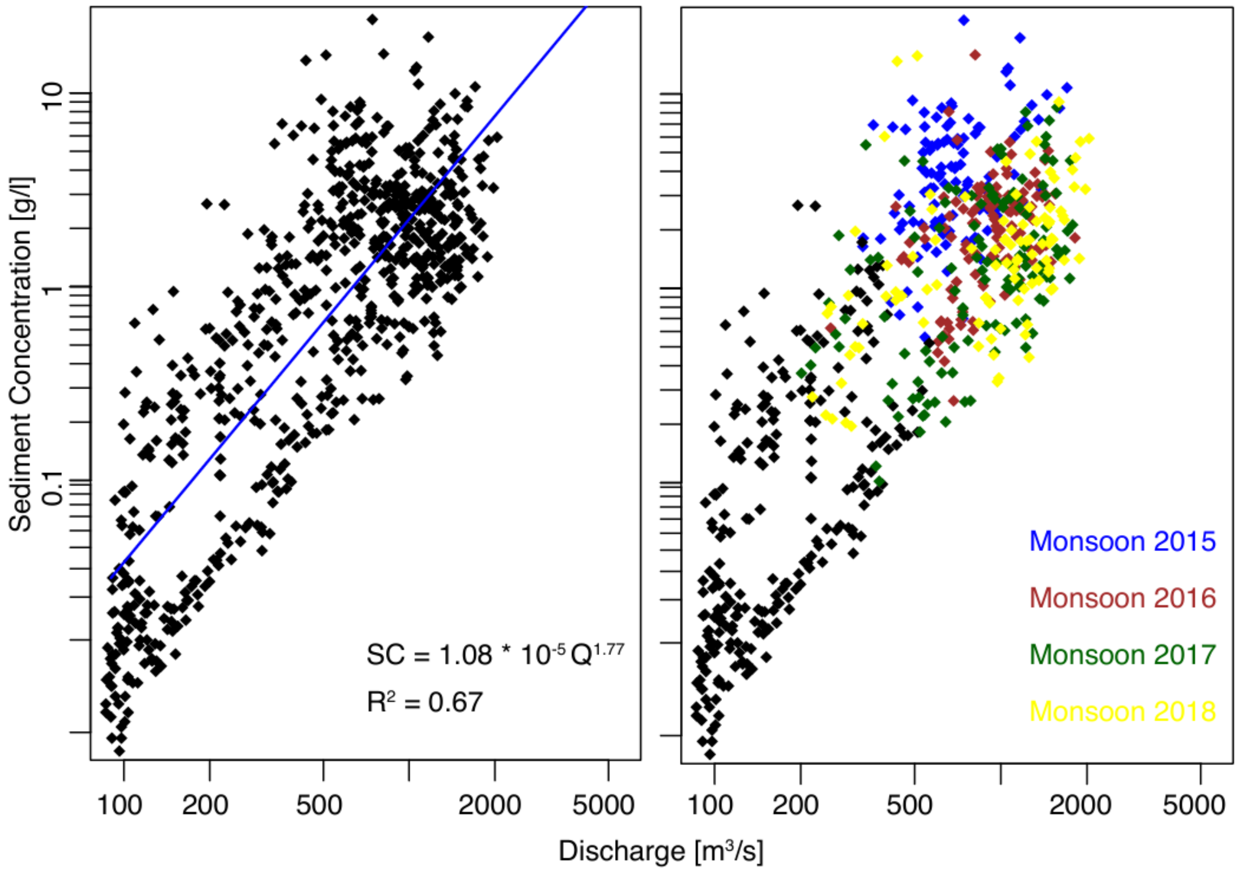

Figure S8: Relationship of sediment concentration and discharge for the entire sampling period at Sunkoshi.

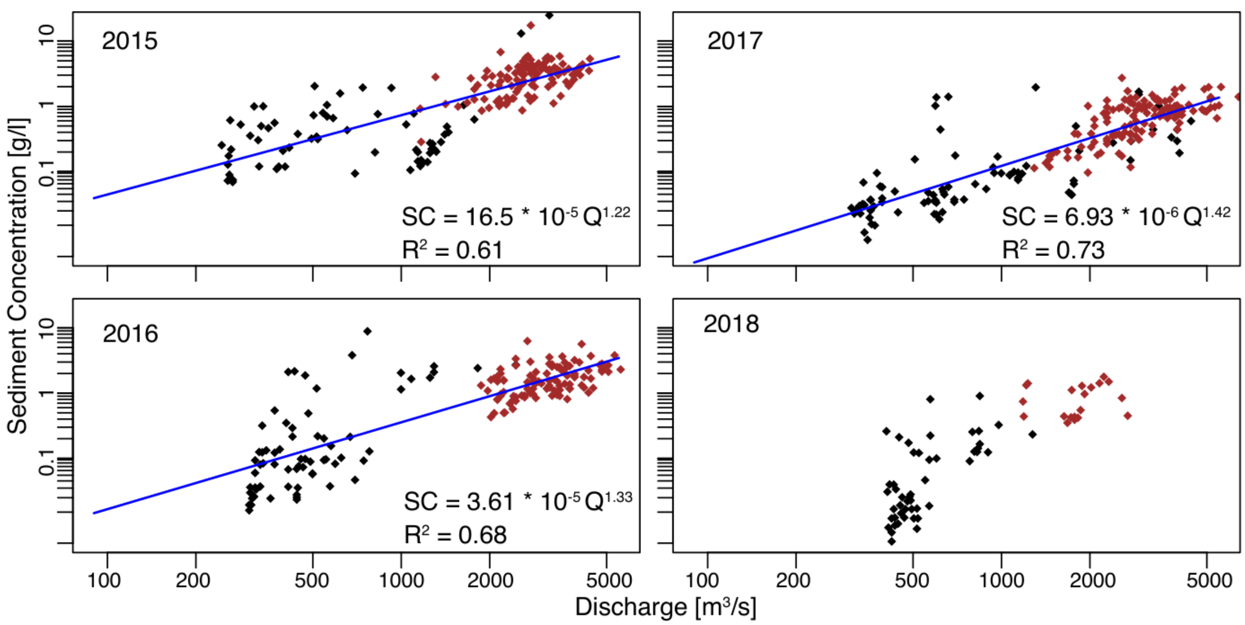

Figure S9: Relationship between sediment concentration and discharge for Saptakoshi sampling station. Red dots indicate samples taken during the monsoon period. No power law relationship for 2018 data has been calculate due to data coverage only extending until June.

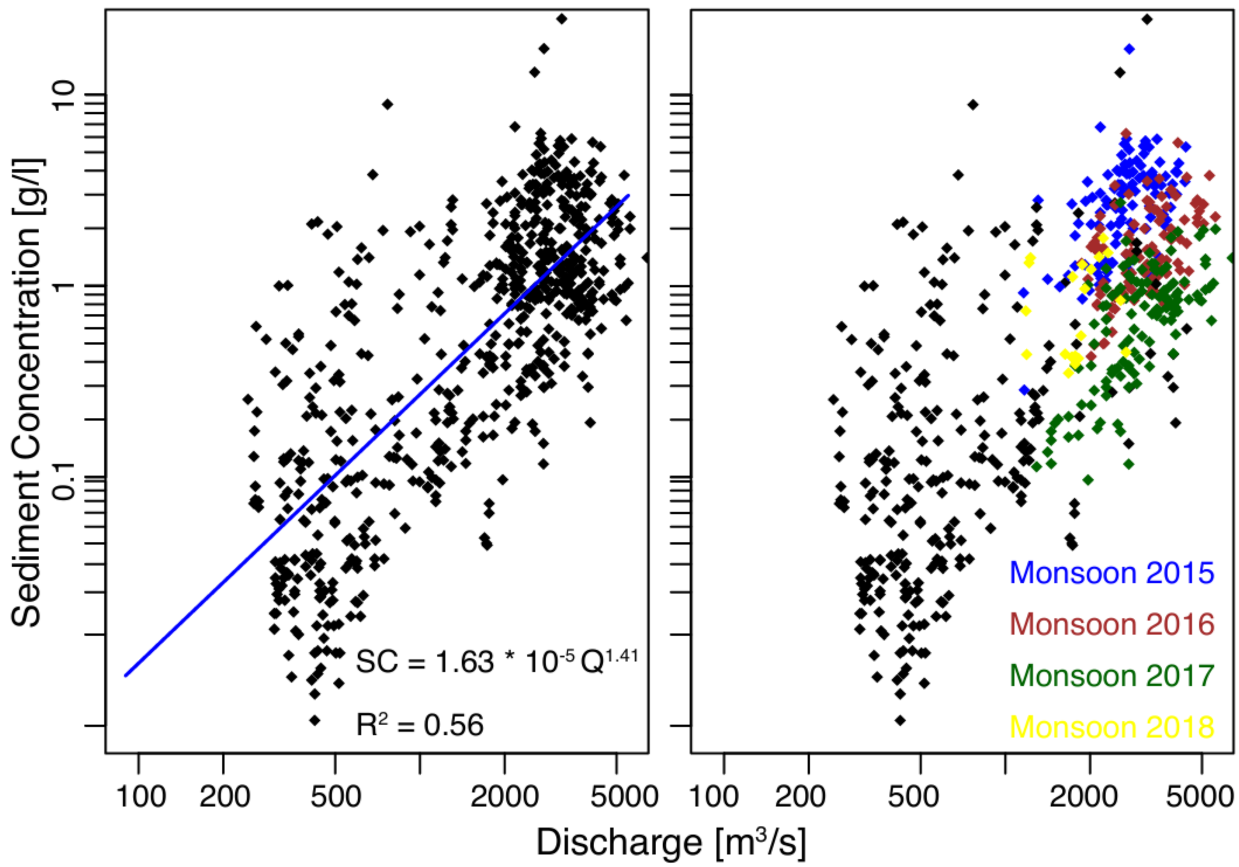

Figure S10: Relationship of sediment concentration and discharge for the entire sampling period at Saptakoshi.

3. Grain size variability of suspended sediment samples

This figure below (S11) serves as complement for figures 5 to 8 presented in the main text. While this figure has a fixed bin interval for each sample, avoiding overrepresentation of isolated samples.

Additionally, we present raw grain size distributions for each monsoon period for each suspended sediment sampling station (Fig. 12).

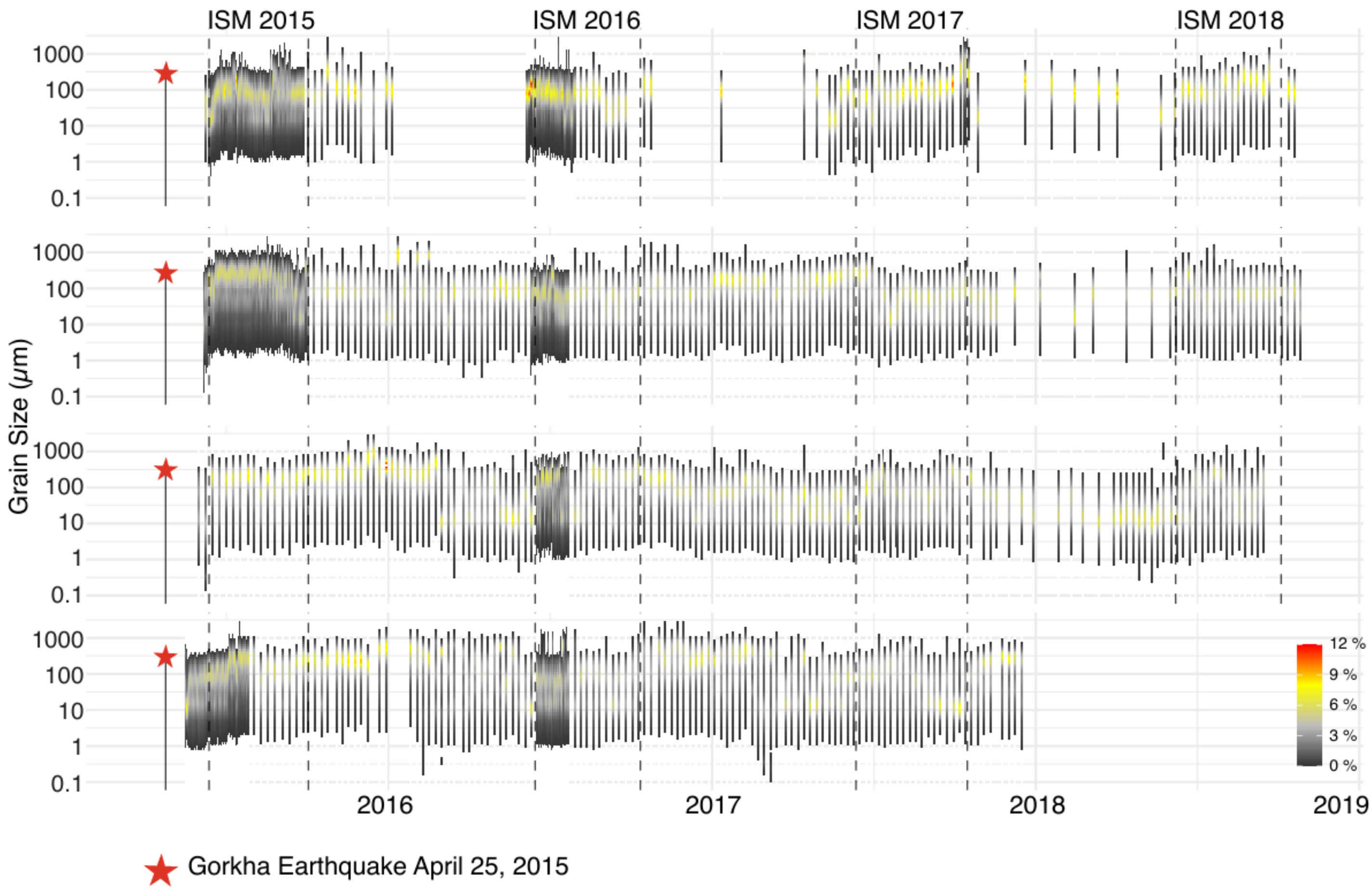

Figure S11: Grain size distribution time series for all four sampling stations. Grain size distributions are expressed as heat plots, where high shares in certain grain size ranges, peaks in the distribution, are displayed in bright color. Vice versa, low shares are represented in dark colors. Data is based on daily suspended sediment samples. Note a logarithmic scale on the y-axis. ISM stands for Indian Summer Monsoon.

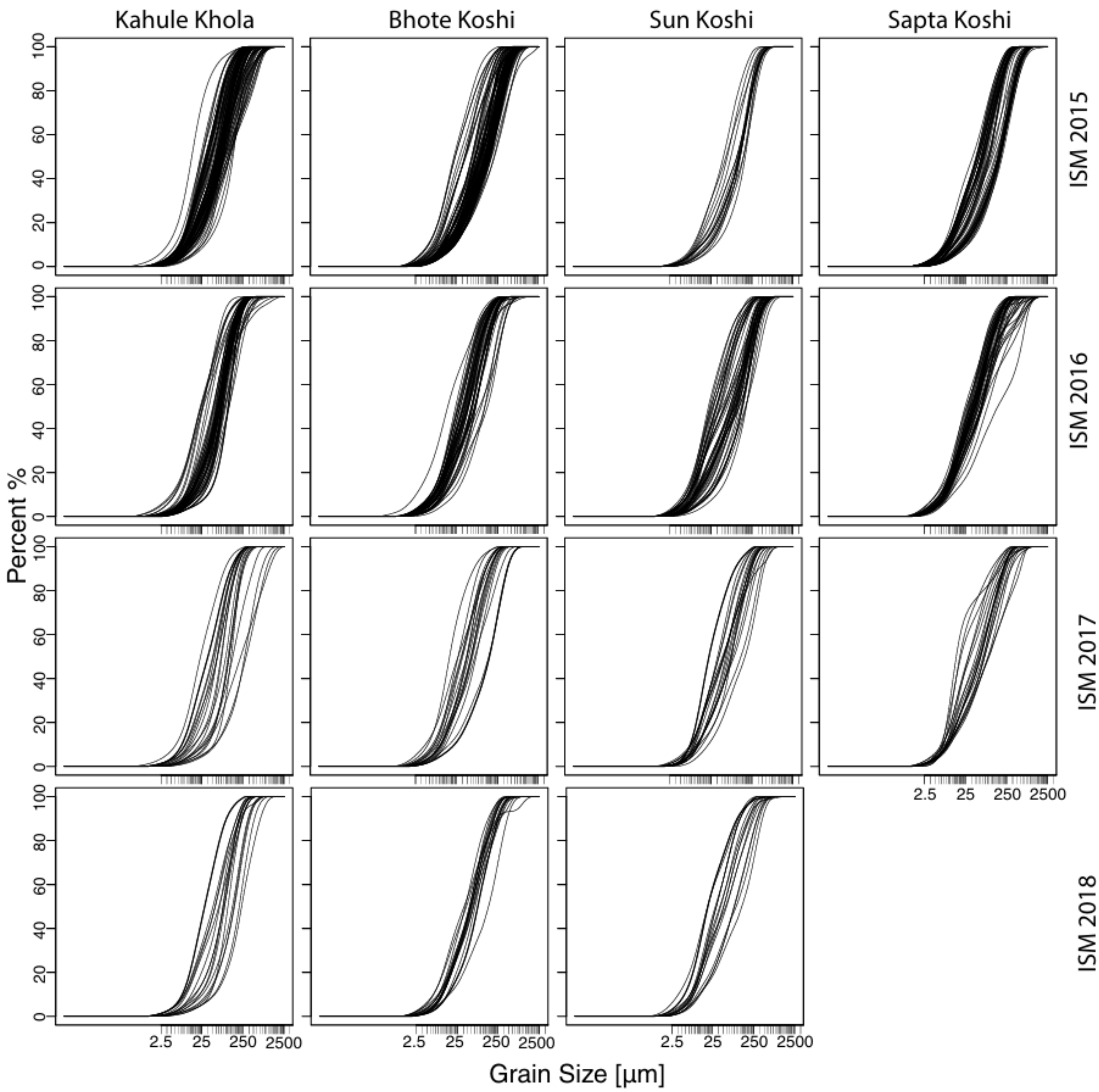

Figure S12: Cumulative density plots of Indian Summer Monsoon (ISM) grain size distribution for each sampling station. The figure is organized as column represents sampling stations and rows illustrate respective monsoon seasons.

4. End-member modelling

This section provides additional details to the end-member modelling analysis conducted in this study. In particular, it describes the process of end-member number selection through different end-member scenarios in more detail. The robust end-member protocol (Dietze and Dietze, 2019a) calculates end-member scenarios based on a minimum and maximum number of possible end-members determined in earlier steps through function get.l and get.q (Dietze and Dietze, 2019a, 2019b). Here the different end-member scenarios are presented for all data sets.

Figure S13 shows different modelled end-member scenarios for all suspended grain size data sets. The determined number of end-members ranged from a minimum of 2 to 8 or 7 in the case of Sunkoshi. Clusters of main end-member modes across the entire range of possible end-member scenarios is illustrated through a kernel density estimate shown as a black line. This led to a detection of four end-members for Kahule Khola and five end-members for the remaining stations. However, especially for Saptakoshi clusters of end-member modes are the least distinct among all sampling stations. Here, unmixing bears the greatest uncertainty. Generally, low number of end-members tend to produce wavey, broad curves, while high number of end-members leads to spikey loadings (Dietze and Dietze, 2019a). Based on these end-member scenarios manual limits of end-member where chosen which are presented in table S2. These mode limits were used to determine robust end-members for each station as described in the methods section in the main text.

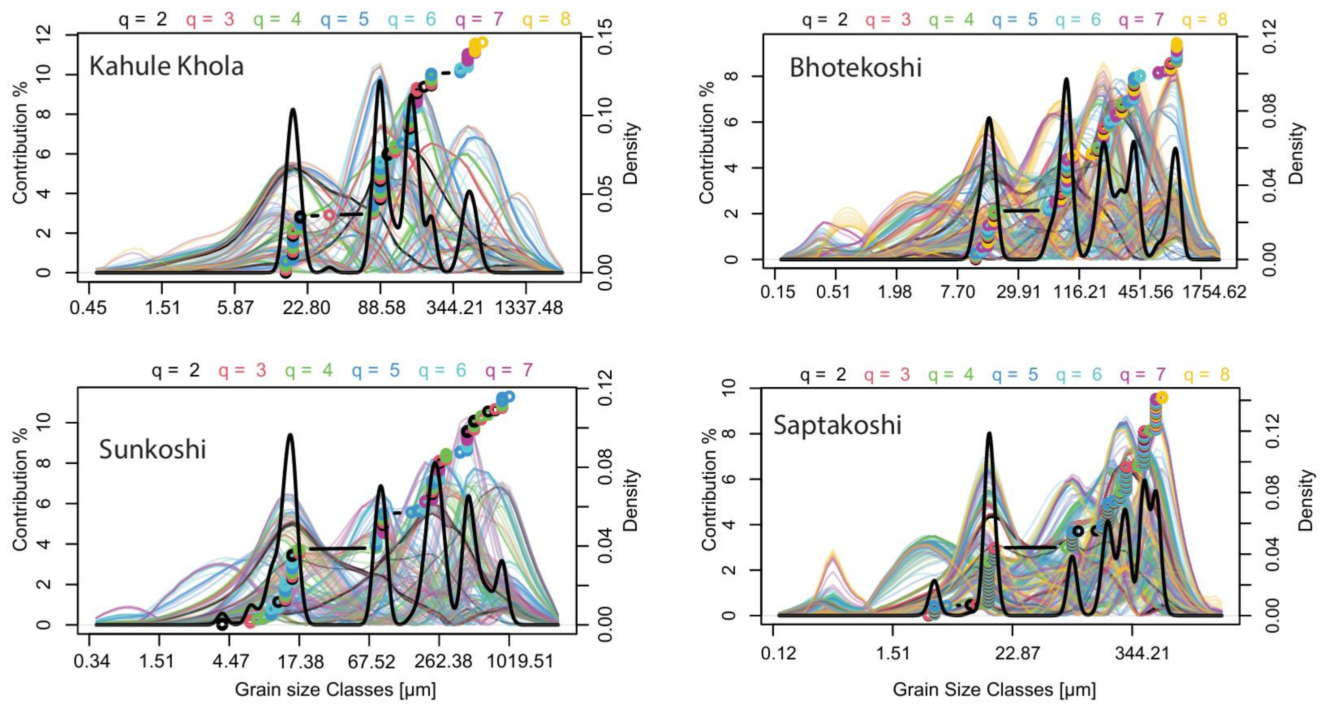

Figure S13: For all plots different colors correspond to different end-member scenarios ranging from minimum to maximum possible end-members. The black line is a kernel density estimate with a default kernel bandwidth of 1% of the number of grain-size classes of the input data set. Colored dots are representative of the main mode positions.

Figure S14 shows different end-member scenarios for grain size data sets of different sediment source types. The determined number of possible end-members ranged from a minimum of 2 to 6 or 7. Unmixing of these data sets is based on much less measurements than compared to the unmixing of the suspended sediment grain sizes, which possibly leads to less reliable results (Dietze et al., 2022). Again, clusters of main end-members modes across the entire range of possible end-member scenarios are illustrated through a kernel density estimate shown as a black line. This informed the detection of the end-members from each data set. Based on these end-member scenarios manual limits of end-member modes were chosen which are presented in table S2.

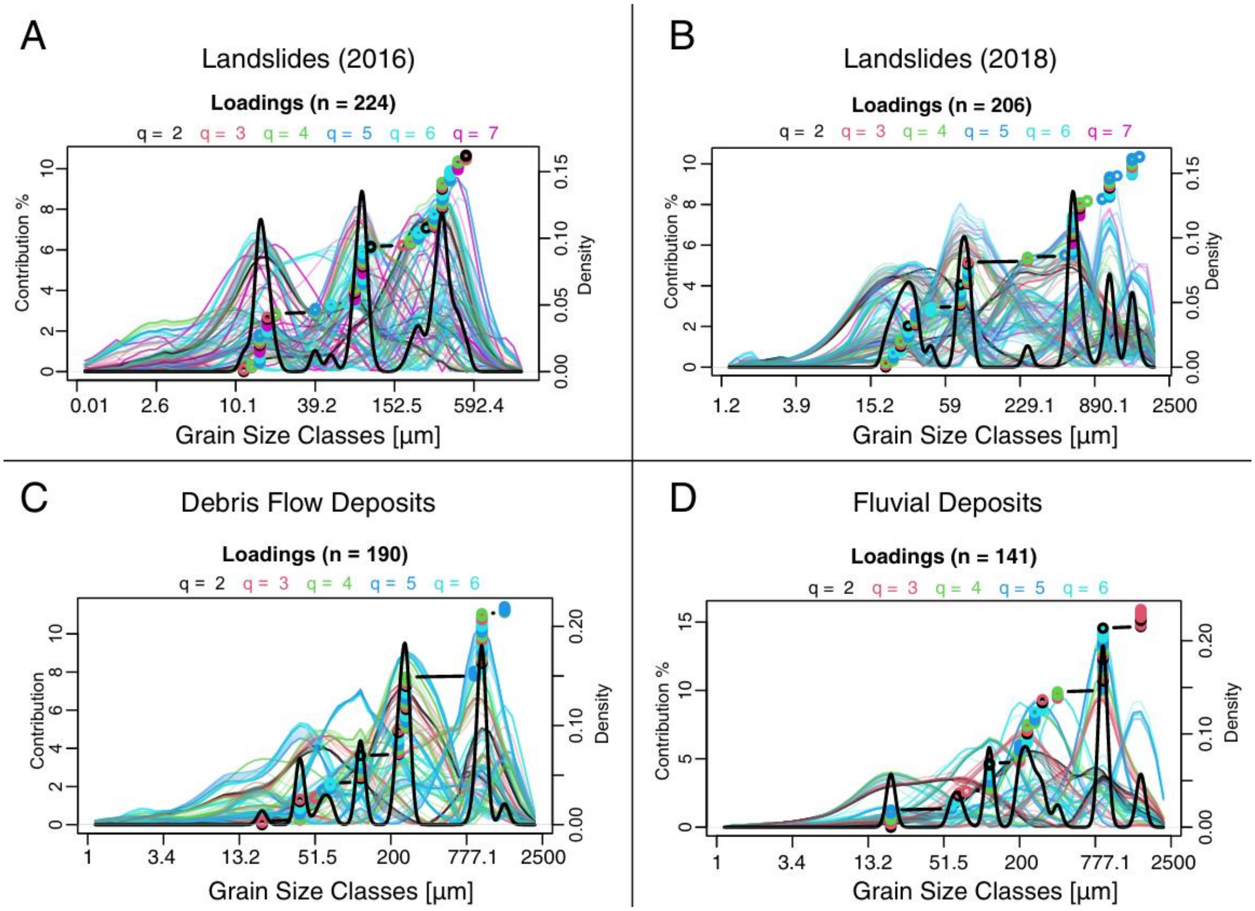

Figure S13: For all plots different colors correspond to different end-member scenarios ranging from minimum to maximum possible end-member scenarios. The black line is a kernel density estimate with a default kernel bandwidth of 1 % of the number of grain-size classes of the input data set. Colored dots are representative of the main mode positions.

Figures S15 and S16 illustrate all raw grain size distribution for suspended sediment samples (Fig. S15) and sediment source types (Fig. S16). Additionally, end-member loadings derived from the end-member modelling are added to the raw grain size distributions. This

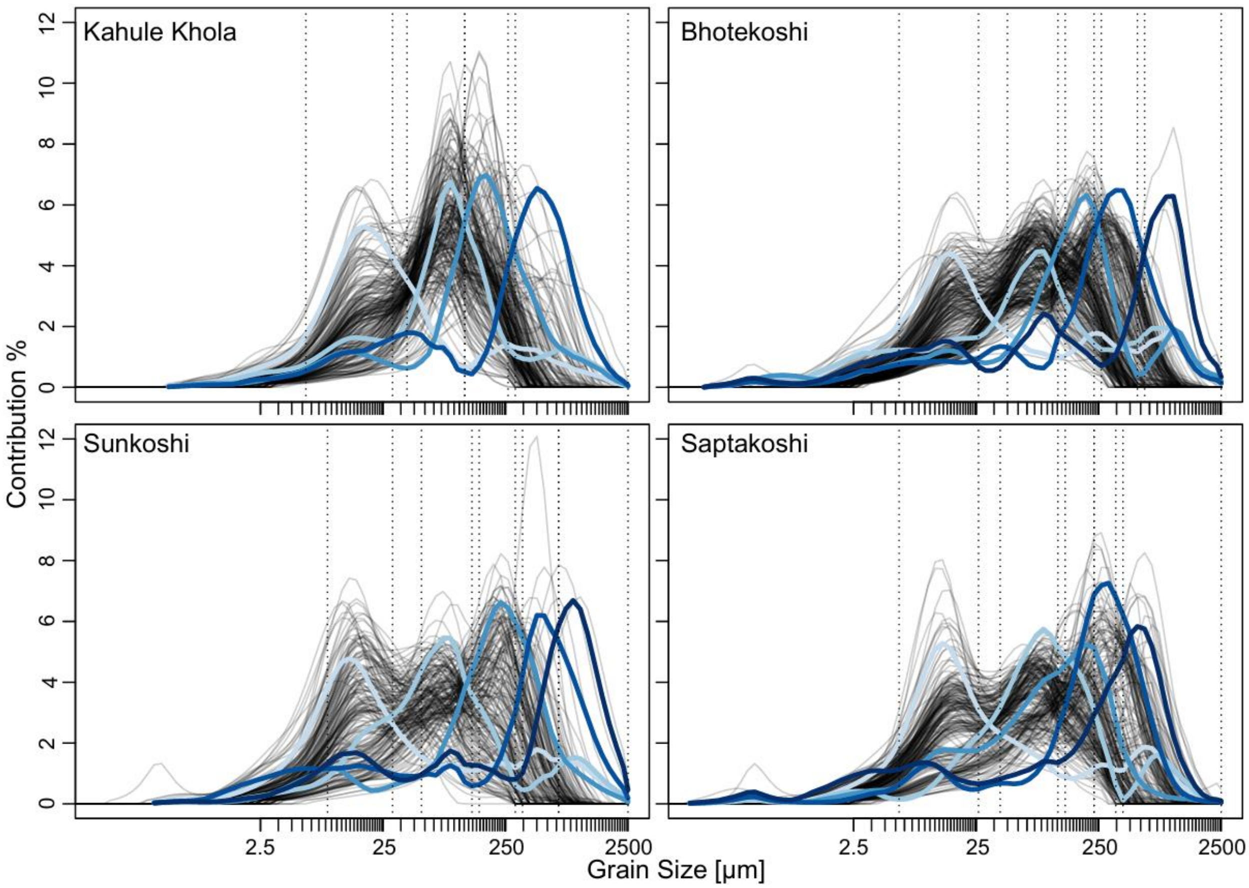

Figure S15: This figure shows raw grain size distribution of all suspended sediment samples from each station. End-members derived from the end-member modelling in previous steps are plotted in their corresponding colors as shown in figure 2 of the main text.

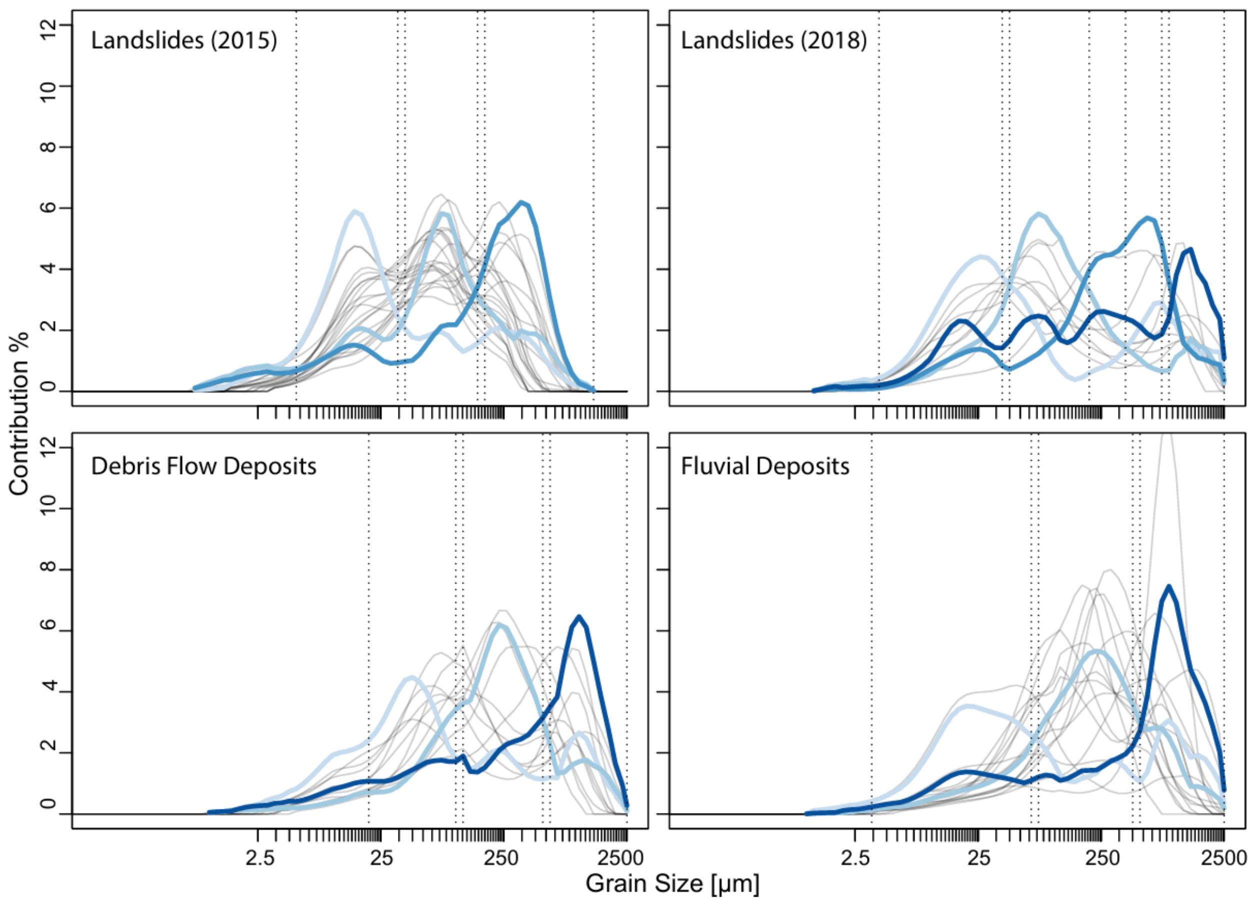

Figure S16: This figure shows raw grain size distribution of all samples from different sediment source types. Respective end-members derived from the end-member modelling in previous steps are plotted in their corresponding colors as shown in figure 3 of the main text.

Table 2: Grain size ranges for all end-members delineated for every data set. Those depict the specified limits chosen in robust end-member protocol. Units of end-member limits are in micrometer.

	End-member 1 (EM1)	**End-member 2 (EM2)**	**End-member 3 (EM3)**	**End-member 4 (EM4)**	**End-member 5 (EM5)**
Kahule Khola	8.8 – 29.9	51.5 - 116.2	133.1 – 300.5	394.2 – 2500.0	-

Bhote Koshi	5.9 – 26.1	44.9 – 116.2	133.1 – 229.1	262.4 – 517.2	592.4 – 2500.0
Sun Koshi	3.9 - 13.2	22.8 – 59.0	67.5 – 133.1	152.5 – 300.5	300.5 – 1167.7
Sapta Koshi	5.9 – 26.1	39.2 – 116.2	133.1 – 229.1	229.1 – 344.2	394.2 – 2500.0
Landslides (sieved)	5.1 – 34.3	39.2 – 152.5	174.6 – 1337.5	-	-
Landslides (sampled 2018)	3.9 – 39.2	44.9 – 200.0	394.2 – 777.1	890.1 – 2500.0	-
Debris flow	19.9 – 1001.5	116.2 – 517.2	592.4 – 2500.0	-	-
Tributaries	3.5 – 67.5	77.3 – 451.6	517.2 – 2500.0	-	-

Figures below show temporal pattern of relative distribution of each end-member to each sample, referred to as end-member scores of every hydrologic sampling station. Figures S17 to S20 are complementary to figures 5 to 8 in the main text, which only present scores of end-member 4 for each sampling site.

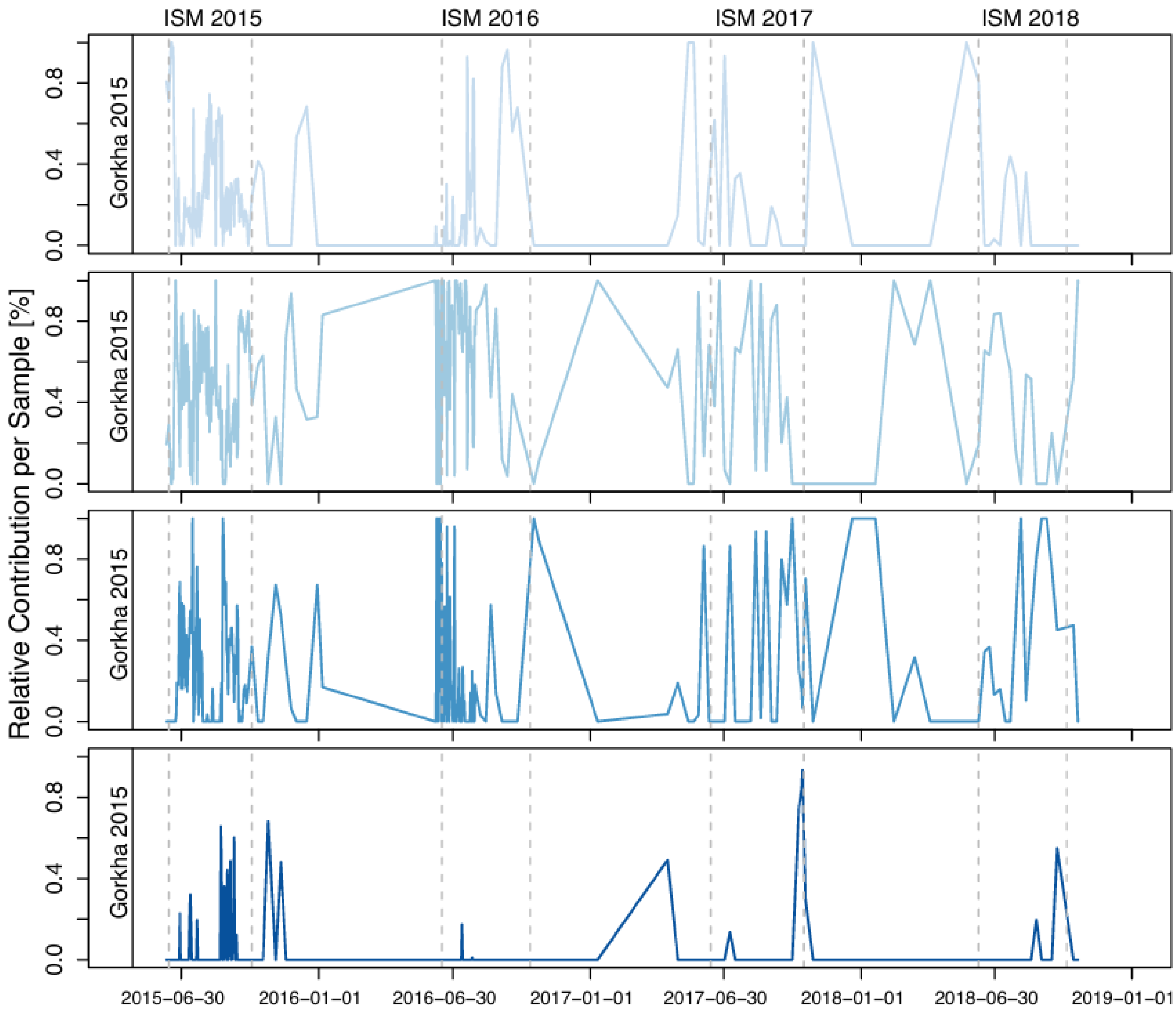

Figure S17: Temporal distribution of end-members for Kahule Khola. Panels from top to down show temporal variability of EM1-4

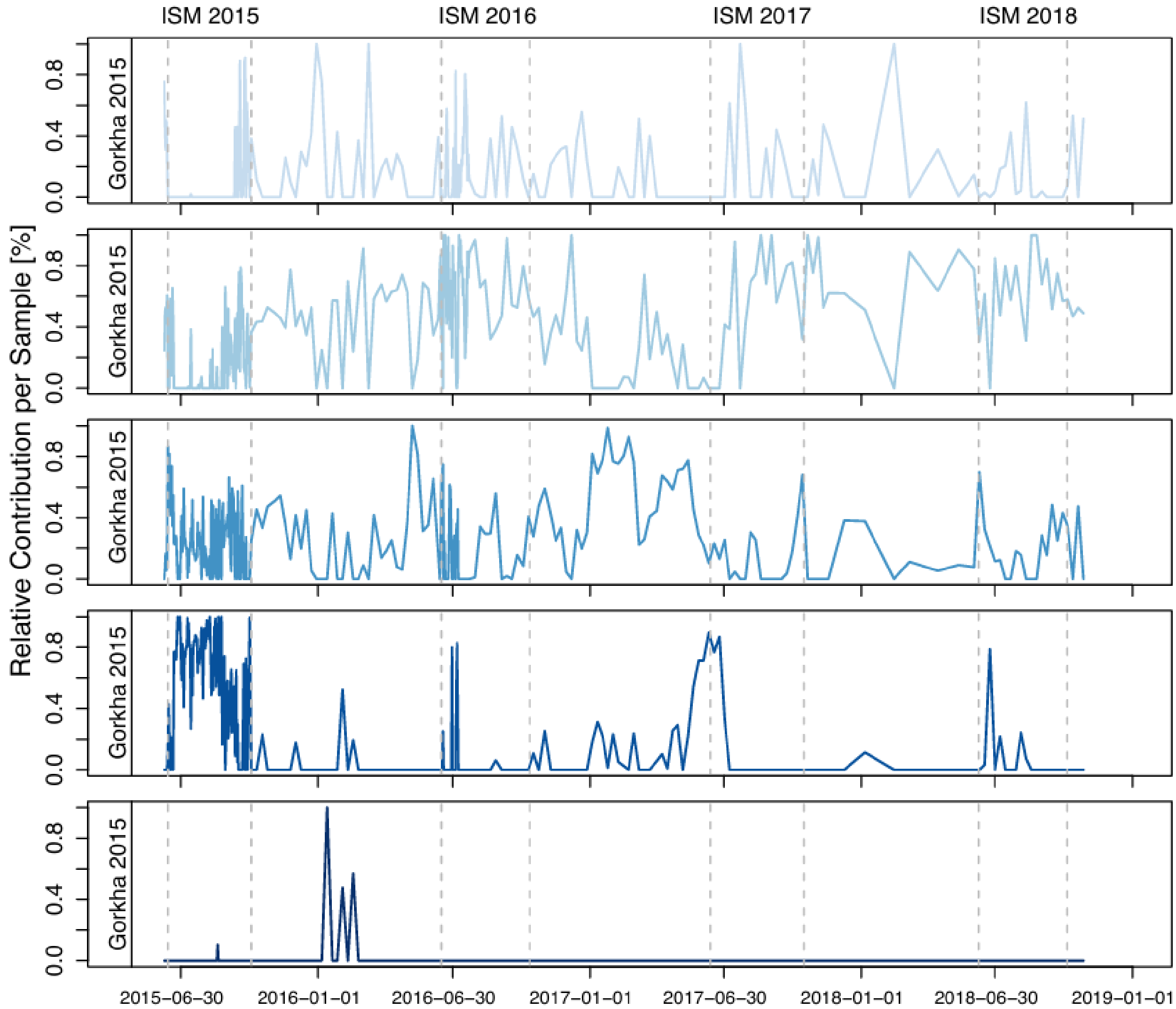

Figure S18: Temporal distribution of end-members for Bhotekoshi. Panels from top to down show temporal variability of EM1 – 5.

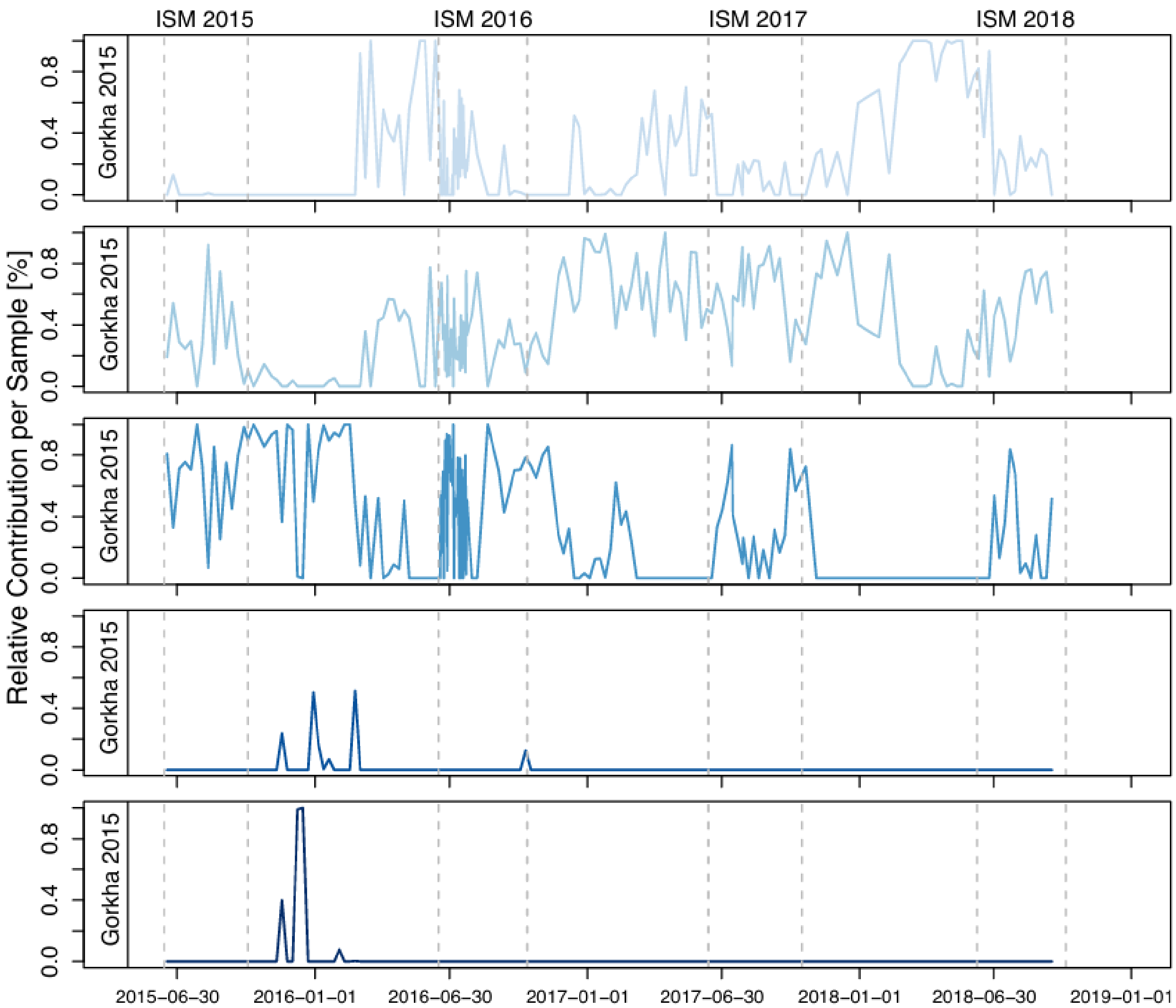

Figure S19: Temporal distribution of end-members for Sunkoshi. Panels from top to down show temporal variability of EM1 – 5.

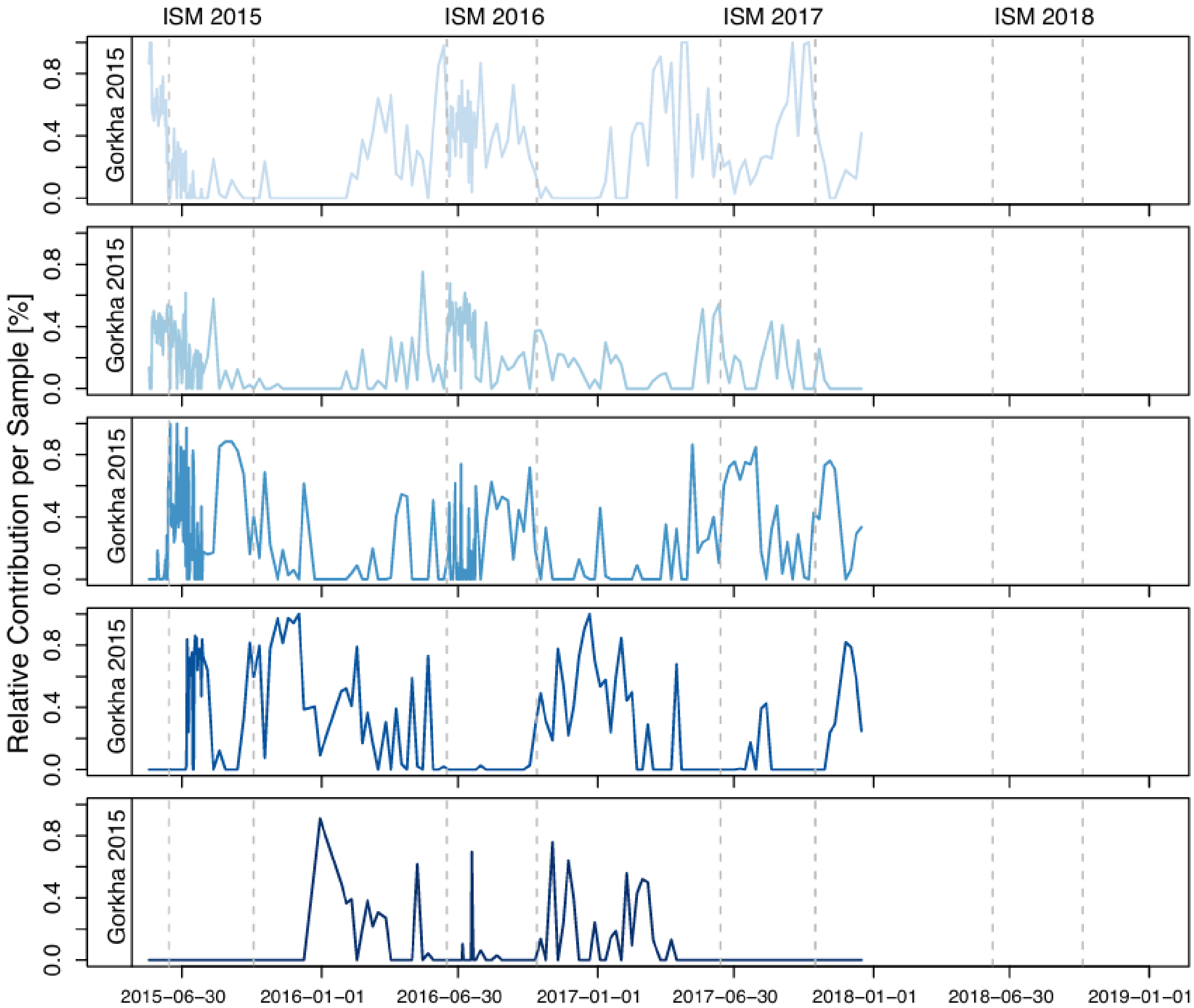

Figure S20: Temporal distribution of end-members for Saptakoshi. Panels from top to down show temporal variability of EM1 – 5.

References

- Anderson, M.J. (2017). Permutational Multivariate Analysis of Variance (PERMANOVA). In Wiley StatsRef: Statistics Reference Online (eds N. Balakrishnan, T. Colton, B. Everitt, W. Piegorsch, F. Ruggeri and J.L. Teugels). https://doi.org/10.1002/9781118445112.stat07841
- British Geological Survey (2022): Simplified Geological Map of central-eastern Nepal (NERC Grant NE/L002582/1). https://webapps.bgs.ac.uk/services/ngdc/accessions/index.html#item165666. Last access: 2025-06-12
- Dietze, E. & Dietze, M. (2019a). Grain-size distribution unmixing using the R package EMMAgeo. E&G Quaternary Science Journal, 68(1):29–46.
- Dietze, E and Dietze, M. (2019b). EMMAgeo. GFZ Data Services. R package version 0.9.8. http://doi.org/10.5880/GFZ.4.6.2019.002.
- Dietze, M., Schulte, P., & Dietze, E. (2022). Application of end-member modelling to grain-size data: Constraints and limitations. *Sedimentology*, *69*(2), 845–863. https://doi.org/10.1111/sed.12929